



Modelling the historical and future evolution of multiple ice masses in the western Tien Shan, Central Asia, using a 3D ice-flow model

Lander Van Tricht^{1,*}, Philippe Huybrechts¹

¹Earth System Science & Departement Geografie, Vrije Universiteit Brussel, Brussels, Belgium

5

Correspondence to: Lander Van Tricht (lander.van.tricht@vub.be)

Abstract. High Mountain Asia (HMA) contains the largest concentration of glaciers outside the polar regions. These glaciers play an essential role in terms of water supply for the surrounding densely populated dry lowland areas. The retreat of glaciers and ice caps in this region can consequently have a major impact on societies. However, few modelling studies exist that examine in detail how individual ice bodies in the area are responding to climate change. Further, different climatic and topographic settings ensure a heterogenous impact of climate change on ice masses in the area. In this study, we focus on the western and central part of the Tien Shan Mountain range in the northwest of HMA. We use several measurements and reconstructions of the ice thickness, surface elevation, surface mass balance and ice temperature to study in detail six different ice bodies in the Kyrgyz Tien Shan: five valley glaciers and one ice cap. The selected ice masses are located in different sub-regions of the Tien Shan with different climatic settings, and they are all characterised by detailed recent glaciological measurements. A 3-dimensional higher-order thermomechanical ice-flow model is calibrated and applied to simulate the evolution of the ice masses since the Little Ice Age and to make a prognosis of the future evolution up to 2100 under different CMIP6 SSP climate scenarios. Further, projections of the total runoff of the ice masses are calculated. The results of this study reveal a strong retreat of most of the ice masses under all climate scenarios, however with important differences. These can be related to the specific climate regime of each of the ice bodies and their geometry. It is highlighted that because the main precipitation occurs in spring and early summer, the ice masses respond to climate change with an accelerating retreat.

10

15

20

1 Introduction

The Tien Shan is one of the largest mountain systems in Asia, stretching for over 3000 km from west to east. The mountain range is, despite its rather low amount of precipitation, heavily glaciated with one of the greatest concentrations of glaciers and ice caps on Earth (Aizen et al., 2006). Projection of the future extent and volume of ice masses in the Tien Shan is of major interest. The aridity in the area and the surrounding regions ensures that during the dry periods in spring and summer, when water sources such as snow melt have been depleted and precipitation is absent, glacial meltwater accounts for a significant proportion of the water supply (Immerzeel et al., 2010; Sorg et al., 2012; Farinotti et al., 2015; Pritchard, 2019). The meltwater is used for drinking, in industry and for irrigation. Glaciers and ice caps in the Tien Shan are therefore essential for the

25



30 streamflow regimes of rivers draining to the populated arid lowlands of Kyrgyzstan, Kazakhstan, Uzbekistan, Turkmenistan
and the Chinese Xinjiang province. A decrease of meltwater in the future will inevitably lead to water deficits and water
scarcity (Sorg et al., 2012; Huss and Hock, 2018). Another subject for which a future prognosis of the ice volume is important
concerns the assessment of the danger of rapid drainages from (pro)glacial lakes and more frequent flow and debris flood
events due to more extreme runoff in spring (Hagg et al., 2006; Sorg et al., 2012; Narama et al., 2018; Compagno et al., 2022).

35

As in many other mountain areas in the world, glaciers in the Tien Shan mountains have retreated significantly since the end
of the Little Ice Age (LIA), and especially since the seventies (Solomina et al., 2004; Immerzeel et al., 2010; Farinotti et al.,
2015; Kraaijenbrink et al., 2017; Shaghedanova et al., 2020; Compagno et al., 2022). However, previous research of glacier
responses showed a non-uniform pattern in the area. For example, glacier shrinkage appeared to be less severe in the continental
40 inner ranges than in the more humid outer ranges because mass turnover of these more continental glaciers is smaller (Sorg et
al., 2012). Further, in some areas, heterogeneously changing precipitation rates led to diverging melt rates. Another reason for
the non-uniform response is the presence or absence of a debris cover insulating the ice below and shielding it from intense
solar irradiance. The variety of responses to climate change complicates general statements about the future evolution of
glaciers in the Tien Shan and stimulates conducting detailed studies to understand the importance of different processes.

45

In this study, we model the future evolution of five glaciers and one ice cap under different CMIP6 SSP climate scenarios
using a 3-dimensional higher-order thermomechanical ice-flow model. The selected model has already been successfully
applied to different ice masses ranging from mountain glaciers (Zekollari et al., 2014; Van Tricht and Huybrechts, 2022) to
ice caps (Zekollari et al., 2017) and an entire ice sheet (Fürst et al., 2011,2013). The six different ice bodies are located in
50 different sub-regions of the western Tien Shan with different climatic settings, and they are all characterised by recent
glaciological measurements which are used for calibration and validation (Hoelzle et al., 2017; Satylkanov, 2018; Van Tricht
et al., 2021a; Van Tricht and Huybrechts, 2022). First, a historical reconstruction is made to correctly capture the past evolution
because today's ice masses are still reacting to past climatic conditions. Hence the ice-flow model is dynamically calibrated
with temperature and precipitation observations since the end of the LIA. Then, from 2022 onwards, the different climate
55 scenarios with data up to 2100 are imposed and the evolution of the ice masses is studied in detail. Projections of the total
runoff are made for each ice mass.

2 Location and climate

60 2.1 Selected ice masses

The Ashu-Tor glacier (42.05°N, 78.17°E) is positioned on the southern slopes of the Terskey Ala-Too Mountain range, south
of Lake Issyk-Kul. This south-facing glacier is situated in the Arabel Plateau highland area. Surface mass balance (SMB)



65 measurements were performed for a short period of time (2014-2019) on the lowest 200 m of the glacier. These measurements are used to calibrate the mass balance model (see section 3.2). The ice thickness of the Ashu-Tor glacier has been measured and reconstructed in 2019. The measurements showed maximum thicknesses up to more than 200 m with a volume of about 0.43 km³ (Van Tricht et al., 2021a). The glacier has a limited altitudinal range of only 600 metres (Table 1).

70 The Bordu (41.81°N, 78.17°E) and Sary-Tor (41.83°N, 78.18°E) glaciers are located in valleys next to each other at the north-western side of the Ak-Shyirak massive. Both glaciers are situated at the southern edge of the Arabel Plateau highland area. On both glaciers, surface mass balance measurements are carried out annually by the Tien Shan High Mountain Scientific Research Centre as part of the CHARIS project (Contribution to High Asian runoff from Ice and Snow/Ice and snow contribution to the flow of High Asia) (Satylkanov, 2018), which are also submitted to the World Glacier Monitoring Service (WGMS). The ice thickness of the Bordu glacier was measured in 2017 and 2019 revealing a maximum thickness of 148 m and an ice volume of about 0.33 km³ (Van Tricht et al., 2021a). The ice thickness of the Sary-Tor glacier was measured in 75 2013 and the measurements showed a maximum ice thickness of 159 m and a volume of ca. 0.15 km³ (Petraikov et al., 2014) (Table 1). Next to that, the Sary-Tor glacier was shown to be a polythermal glacier with a large part of temperate ice over the bed. This was proven by both measurements and modelling (Petraikov et al., 2014; Van Tricht and Huybrechts, 2022). The specific thermal structure could be explained by the release of heat through the refreezing of meltwater in the accumulation 80 area, and due to the insulation of snow during the winter months.

The Grigoriev ice cap (41.96°N, 77.91°E) is a small ice cap (also called flat top glacier), situated at approximately 30 km to the northwest of the Bordu and Sary Tor glaciers. The more or less circular ice cap is located at a high altitude, primarily between 4200 and 4600 m. The ice thickness of the ice cap was measured in 2021 by Van Tricht and Huybrechts (2022) who 85 showed a maximum thickness of 114 m and a volume of about 0.39 km³ (Table 1). The surface mass balance has been measured and reconstructed for different time periods (Mikhalevko, 1989; Dyurgerov, 2002; Arkhipov et al., 2004; Fujita et al., 2011). These measurements are used for calibration of the mass balance model. Similar to the Ashu-Tor glacier, the Grigoriev ice cap has a very small altitudinal range of only 400 m when the outlet glaciers at the eastern side are excluded. Several deep ice cores were made in the past measuring the ice temperature (Dikikh, 1965; Thompson et al., 1993; Arkhipov et al., 2004; 90 Takeuchi et al., 2014). These measurements were used to calibrate and model the thermal regime of the ice cap, which showed that the Grigoriev ice cap consists of cold ice cap except for a thin layer at the contact between the ice and the bedrock over the central part which might be characterised by a layer of temperate ice (Van Tricht and Huybrechts, 2022).

The Golubin glacier (42.46°N, 74.47°E) is situated approximately 500 km to the west of the 4 previous ice masses. More 95 specifically, this glacier is located in the Ala-Archa catchment in the Kyrgyz Ala-too range in the north-western Tien Shan. In 2019, the glacier covered an area of 4.6 km² with a volume of about 0.30 km³ (Van Tricht et al., 2021a). The maximum measured ice thickness was 154 m (Table 1). Glaciological investigations on the Golubin glacier started in 1958 and continued



until 1994. In 2010, mass balance measurements were re-initiated in the framework of the Capacity Building and Twinning for Climate Observing Systems (CATCOS) and Central Asia Water (CAWa) projects, and they continue today (Hoelzle et al., 2017). For unmeasured years, the mass balance has been reconstructed using a temperature index model and snowline observations (Barandun et al., 2018; Azisov et al., 2022), showing a steepening of the ablation and accumulation gradients in the past two decades. Nowadays, the glacier front is located at about 3400 m a.s.l. while the upper areas reach elevation of about 4300 m a.s.l., meaning that the glacier consists of an elevation range of 900 m (Table 1).

The Kara-Batkak glacier (42.15°N, 78.27°E) is a small reference glacier in the Inner Tien Shan. The Kara-Batkak glacier is located at the northern slopes of the Terskey Ala-Too Mountain range south of Lake Issyk-Kul. The Kara-Batkak glacier is one of the few glaciers in the area with a relatively large amount of data with a mass balance series dating back to 1957. The surface mass balance measurements continued up to 1998. In 2013, the measurements were reinitiated as part of the CHARIS Project (Satylkanov, 2018). Van Tricht et al. (2021a) measured and reconstructed the ice thickness showing a maximum of 113 m and they determined the glacier volume to be about 0.10 km³ in 2017. The Kara-Batkak glacier is characterised by a large altitudinal range of 1300 m (Table 1).

Table 1. Overview of the main characteristics of the selected ice masses. The length of the Grigoriev ice cap corresponds to the length of the largest cross section.

	Ashu-Tor	Bordu	Golubin	Grigoriev	Kara-Batkak	Sary-Tor
Length (km)	4.81 (2021)	4.24 (2021)	4.95 (2019)	4.53 (2021)	3.46 (2021)	3.83 (2021)
Area (km²)	4.76 (2019)	4.89 (2017)	4.64 (2019)	7.55 (2021)	2.27 (2017)	2.69 (2013)
Max ice thickness (m)	201 (2019)	148 (2017)	154 (2019)	114 (2021)	113 (2017)	159 (2013)
Volume (km³)	0.43 (2019)	0.33 (2017)	0.30 (2019)	0.39 (2021)	0.10 (2017)	0.15 (2013)
SMB measurements	2014 - 2019	2014 - today	1958 – 1994 2010 - today	*	1957-1998 2013 - today	2015 - today
Orientation	SSW	NW	NNW	Mainly SSW	N	NW
Current altitude range	3900 - 4500	3900 - 4700	3300 - 4400	4000-4600	3300 - 4600	3900-4800
Type	Valley glacier	Valley glacier	Valley glacier	Ice cap	Valley glacier	Valley glacier

*Surface mass balance episodically measured (Mikhalenko, 1989; Dyurgerov, 2002; Arkhipov et al., 2004; Fujita et al., 2011).

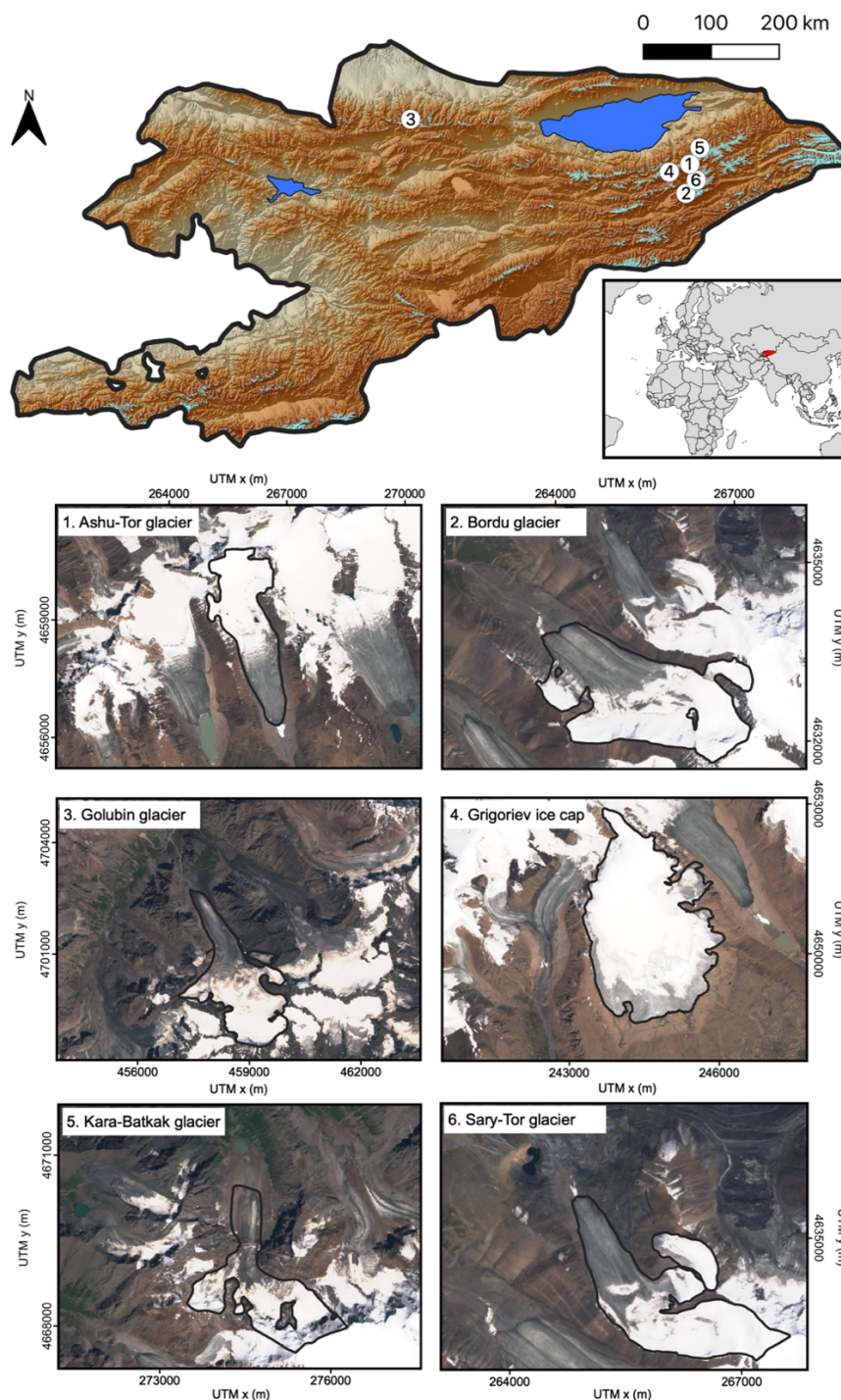


Figure 1: Selected glaciers and their location in Kyrgyzstan. The background satellite images are from Sentinel-2 data. All RGIv6.0. glaciers are shown in pale blue on the upper map. The black outlines of the glaciers in the individual panels show the extent in 2021. The DEM of the upper panel is SRTM.



2.2 Climatic setting and drainage

The continental climate of the Tien Shan is characterised by a strong seasonal variation in precipitation and large amplitudes of air temperatures. Precipitation is highest in spring and summer accounting for about 75% of the annual total. This precipitation is primarily caused by convection and a strengthening of instability caused by cold moist air mass influxes from the west (Aizen, 1995). In winter, the advection of precipitation by westerly flow is blocked by the strong influence of the Siberian High. Hence, winter precipitation accounts for only 8-10% of the annual total (Aizen, 1995). This means that the ice masses are characterised by a simultaneous occurrence of accumulation and ablation in spring and (early) summer, making them very sensitive to temperature changes in spring and summer (Fujita, 2008; Van Tricht et al., 2021b). A rise in temperatures during this period not only causes increased melting, but also a reduction of snow and a decrease in albedo. The Ashu-Tor, Bordu and Sary-Tor glaciers as well as the Grigoriev ice cap, are all located in the Arabel plateau system with a very limited amount of annual precipitation (~320 mm yr⁻¹ at 3600 m a.s.l.) (Van Tricht et al., 2021b). These ice masses feed several of Central Asia's largest rivers such as the Naryn river, which flows in the Syr Darya river, draining westwards towards the Aral Sea basin (Blomdin et al., 2016). The Golubin glacier is located further to the northwest of Kyrgyzstan, in an area which is characterised by a larger amount of annual precipitation, of up to 550 mm yr⁻¹ at 2000 m a.s.l. (Aizen et al., 2006). The greater amount of annual precipitation can be explained by the larger influx of moisture from the northwest, in which direction the Kyrgyz Ala-Too is oriented. Meltwater from glaciers in the area feed the endorheic basin of the Chu River, which is the major irrigation and water supply for northern Kyrgyzstan including the capital Bishkek and the Kazakh steppe. The Kara-Batkak glacier finally is located at the northern slopes of the Terskey Ala-Too which is more exposed to moisture originating from the Issyk-Kul Lake. The glacier area is therefore characterised by a wetter climate (on average 600-700 mm yr⁻¹ at 2600 m a.s.l.) (Van Tricht et al., 2021b). Meltwater from glaciers in this area drains towards the endorheic basin of the Issyk-Kul lake.

2.3 Meteorological data

Three meteorological data series are used to represent the climate near the six different ice masses. The reconstructed data series of Kumtor-Tien Shan (Van Tricht et al., 2021b) is used for the Ashu-Tor glacier, the Bordu glacier, the Grigoriev ice cap and the Sary-Tor glacier. For the Kara-Batkak glacier, the dataset of Chon-Kyzyl-Suu is used. Concerning the Golubin glacier, a meteorological dataset is created for the location of the AWS at 3300 m a.s.l. near the Golubin glacier (Hoelzle et al., 2017). For the latter glacier, directly measured temperatures are used for 2014-2021. For 1961-2013, anomalies derived from measured temperatures at the Ala-Archa station (situated at 2145 m a.s.l. ~10 km from the front of the Golubin glacier) are used. For the 1901-1960 period, data from the CruTEM (Climatic Research Unit gridded land-based TEMperature database) are taken and between 1750 and 1900, data from tree rings are used (see Van Tricht et al. 2021b for more information). For precipitation we rely on ERA5 data, which are scaled to match the measured mean annual precipitation of



155 the Ala-Archa station for the overlapping period, for 1961-2021. The CruTS (Climatic Research Unit gridded Time Series)
dataset is considered for the 1901-1960 period. To represent the precipitation during 1750-1900, data from tree rings are used
(Solomina et al., 2014).

2.4 Little Ice Age

160

Glaciers and ice caps in the Kyrgyz Tien Shan repeatedly advanced and retreated throughout the Holocene. The latest period
of significant advance was caused by the LIA, and it was dated to 1730-1910. In most areas, several moraines belong to the
LIA, indicating different stages of glacial stagnation and advances within this period. However, a majority of terminal and side
moraines were formed in the middle of the 19th century (Solomina et al., 2004; Li et al., 2017). In this study, we consider the
165 1820-1850 average climatic conditions to represent the end of the LIA period.

2.5 Future climate

For the future climate, we rely on climate change projections from multiple global climate models (GCMs) which participated
170 in the sixth phase of the Coupled Model Intercomparison Project 6 (CMIP6) (Table 2), available through the Earth System
Grid Federation (ESGF) archive. Five shared socioeconomic pathways (SSP) are considered which represent a peak and
decline scenario (SSP1-1.9 and SSP1-2.6), two medium scenarios (SSP2-4.5 and SSP3-7.0), and a high emission scenario
(SSP5-8.5). These new climate scenarios have been developed for the Sixth Assessment Report of the Intergovernmental Panel
on Climate Change (IPCC AR6).

175



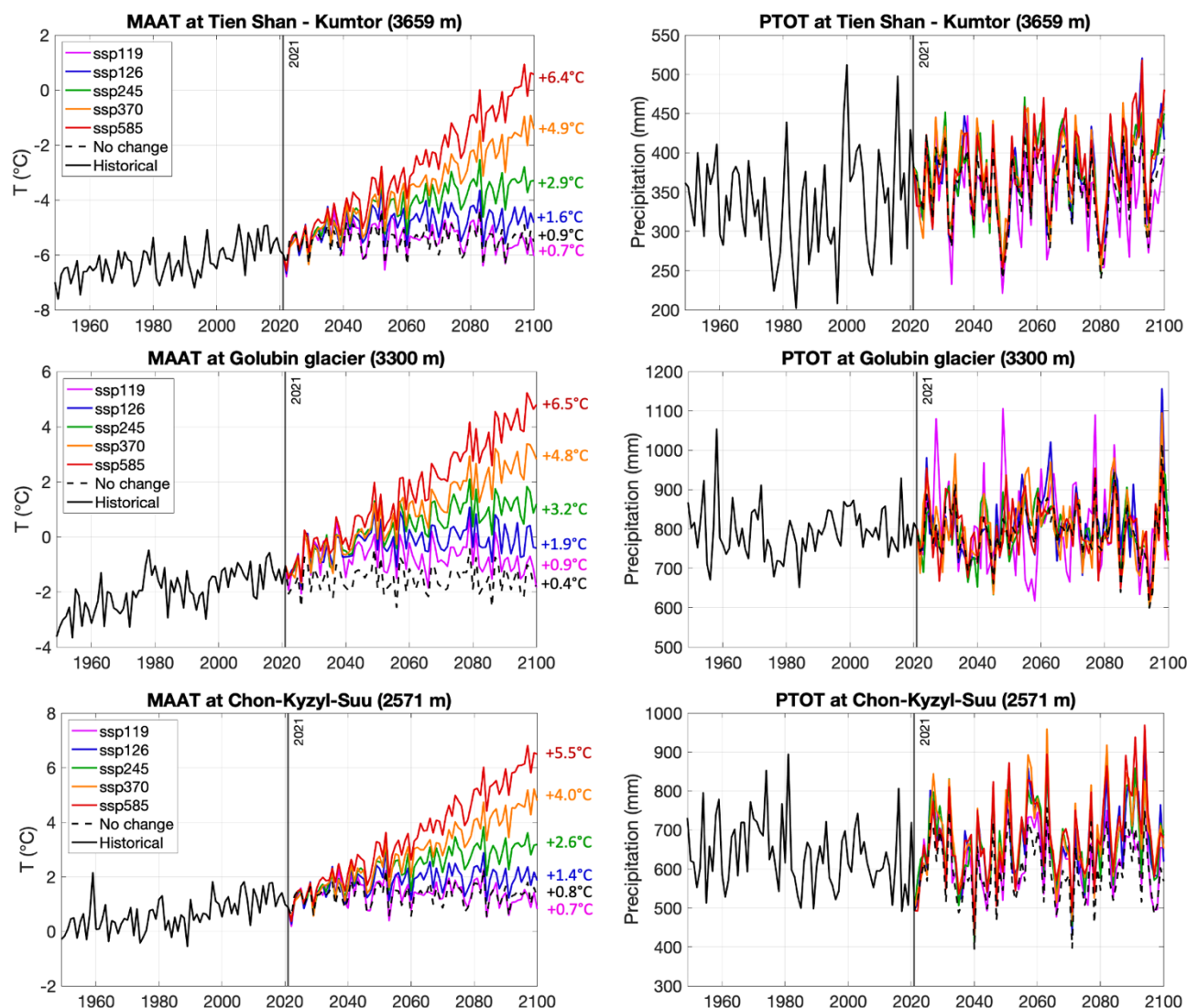
Table 2: CMIP6 global climate models (GCM) used for the climate projections.

GCM	Spatial resolution (lat/lon)	SSP1-1.9	SSP1-2.6	SSP2-4.5	SSP3-7.0	SSP5-8.5
ACCESS-CM2	1.25° X 1.88°		X	X	X	X
ACCESS-ESM1-5	1.25° x 1.88°		X	X	X	X
AWI-CM-1-1-MR	0.93° X 0.94°		X	X	X	X
CAMS-CSM1-0	1.11° x 1.13°	X	X	X	X	X
CanESM5	2.77° X 2.81°	X	X	X	X	X
CanESM5-CanOE	2.77° x 2.81°		X	X	X	X
CAS-ESM2-0	1.42° X 1.41°		X	X	X	X
CESM2	0.94° x 1.25°		X	X	X	X
CESM2-WACCM	0.94° X 1.25°		X	X	X	X
CMCC-CM2-SR5	0.94° x 1.25°		X	X	X	X
CMCC-ESM2	0.94° X 1.25°		X	X	X	X
CNRM-CM6-1-HR	0.50° x 0.50°		X	X	X	X
CNRM-ESM2-1	1.39° X 1.41°		X	X	X	X
E3SM1-1	1.00° x 1.00°					X
E3SM1-1-ECA	1.00° X 1.00°					X
EC-Earth3-CC	0.70° x 0.70°	X		X		X
EC-Earth3-Veg-LR	1.11° X 1.13°	X	X	X	X	X
FGOALS-f3-L	1.00° x 1.25°		X	X	X	X
GFDL-ESM4	1.00° x 1.25°	X	X	X	X	X
HadGEM-3-LL	1.25° x 1.88°		X	X		X
IITM-ESM	1.89° x 1.88°		X	X	X	X
INM-CM4-8	1.50° x 2.00°		X	X	X	X
INM-CM5-0	1.50° x 2.00°		X	X	X	X
IPSL-CM6A-LR	1.27° x 2.50°	X	X	X	X	X
KACE-1-0-G	1.25° x 1.88°		X	X	X	X
KIOST-ESM	1.89° x 1.88°		X	X		X
MIROC6	1.39° x 1.41°	X	X	X	X	X
MPI-ESM1-2-HR	0.93° x 0.94°		X	X	X	X
MRI-ESM2-0	1.11° x 1.13°	X	X	X	X	X
NESM3	1.85° x 1.88°		X	X		X
NorESM2-LM	1.89° x 2.50°		X			X
NorESM2-MM	0.90° x 1.25°		X	X	X	X
TaiESM1	0.94° x 1.25°		X	X	X	X

For every available GCM and every meteorological station, the data are downloaded for both historical runs (1984-2014) and for future projections (2022-2100). The grid cell closest to the meteorological stations is considered. Each GCM has a specific spatial resolution of between 0.50° and 2.88°, corresponding to ca. 55 to 300 km in latitudinal distance (Table 2). The data



185 from every individual GCM are then converted into anomalies for temperature and into ratios for precipitation, with respect to
the overlapping historical period (1984-2014) and scaled to match the standard deviation of the observations of the specific
meteorological datasets (see section 2.3). Then, for every SSP-scenario, the monthly temperature anomalies and precipitation
ratios are averaged over all models resulting in a multi-model mean time series, combining up to 33 different GCMs (see Table
2). In addition, a “No change” scenario is created for which the average climatic conditions of 2001-2021 are repeated until
2100. Subsequently, to account for interannual variability, the data are rescaled using a sequence of historical observations.
190 Finally, as was done for the historical period (Van Tricht et al., 2021b), the monthly data series are downscaled to hourly
resolution by using an observed data sequence. The effect of a lower resolution of the GCMs compared to Regional Climate
Models (RCMs) is expected to be limited as we consider anomalies and because we impose climatic variability based on
observations. Next to that, by combining multiple GCMs, the influence of errors and uncertainties of individual models are
assumed to be reduced strongly, which is beneficial for the reliability of future projections. Only for the SSP1-1.9 scenario, a
195 limited number of GCMs (8) was available at the time of the experiments. For all three meteorological datasets, temperatures
are projected to increase substantially compared to the 2001-2021 mean, with values between +0.7°C for the SSP1-1.9 scenario
and up to +6.5°C for the SSP5-8.5 scenario (Figure 2). The projected evolution of the total precipitation shows a slight but
insignificant increase for the Tien Shan – Kumtor location and no real trend for the two other locations (Figure 2).



200

Figure 2: Evolution of the mean annual air temperature (MAAT) and the yearly total precipitation (PTOT) between 1950 and 2021 as well as projections until 2100 under different climate scenarios for the three locations. The numbers at the right side of the left panels indicate the average warming in 2090-2100 for every scenario with respect to the 1960-1990 average.

205



210 3 Method and models

3.1 Higher-order ice dynamic flow model

A 3-dimensional higher-order thermo-mechanical ice-flow model (3D HO-model) is used to model the ice flow in this study. In the model, both longitudinal and transverse stress gradients are considered (Zekollari et al., 2013), in contrast to Shallow Ice Approximation (SIA) models (Hutter, 1983). The 3D HO-model assumes cryostatic equilibrium in the vertical, implying that vertical resistive stresses are neglected (Pattyn, 2003), in contrast to Full-Stokes models that incorporate all stresses (Jouvet et al., 2011). Further, it is also assumed that the horizontal gradients of the vertical velocity are much smaller than the vertical gradients in the horizontal velocity. This reduces the processing compared to a Full Stokes model as only the horizontal velocity components are solved for. In the following, the applied model is briefly described. A more detailed description of model can be obtained from Fürst et al. (2011).

The vertical velocity component is derived from the incompressibility condition. Nye's generalisation of Glen's flow law (Eq. 1) with a power exponent (n) of 3 is used to quantify the ice deformation and the corresponding flow velocity due to internal deformation based on the stresses that act on it:

$$\tau_{ij} = 2\eta\dot{\epsilon}_{ij} \quad (1)$$

$$\eta = \frac{1}{2}A(T_{\text{pmp}})^{-\frac{1}{n}}(\dot{\epsilon}_e + \dot{\epsilon}_0)^{\frac{1}{n}-1} \quad (2)$$

$$A(T_{\text{pmp}}) = m a \exp\left(-\frac{Q}{RT_{\text{pmp}}}\right) \quad (3)$$

$$\dot{\epsilon}_e^2 = \frac{1}{2}\dot{\epsilon}_{ij}\dot{\epsilon}_{ij} \quad (4)$$

$$\dot{\epsilon}_{ij} = \frac{1}{2}(\partial_i u_j + \partial_j u_i) \quad (5)$$

η is the effective viscosity of the ice (Eq. 2), which is defined via the second invariant of the strain rate tensor (Eq. 4). $\dot{\epsilon}_0$ is a small offset (10^{-30}) that ensures finite viscosity. The symbols 'i' and 'j' represent the space derivative with respect to the i^{th} and j^{th} spatial components. The flow rate factor $A(T_{\text{pmp}})$ is a function of ice temperature with respect to the pressure melting point (Eq. 3). m is an enhancement factor which is used for calibration (see section 4). The tuning of the enhancement factor is an implicit way to include the softening effect due to factors such as water content and impurity content (Huybrechts et al., 1990). For temperatures lower than -10°C , $a = 1.14 \times 10^{-5} \text{ Pa}^n \text{ a}^{-1}$ and $Q = 60 \text{ kJ mol}^{-1}$ while for temperatures larger than -10°C , $a = 5.47 \times 10^{10} \text{ Pa}^n \text{ a}^{-1}$ and $Q = 139 \text{ kJ mol}^{-1}$. R is the gas constant ($8.31 \text{ J mol}^{-1} \text{ K}^{-1}$). T_{pmp} is the ice temperature relative to the pressure melting point (homologous temperature). $\dot{\epsilon}_e^2$ is the effective strain rate as the second invariant of the strain rate tensor.



The strain rate tensor is defined in terms of velocity gradients (Eq. 5) with u the 3-dimensional components of the velocity vector. Further, in the ice flow model, a Weertman-type sliding law is implemented (Eq. 6). Here, the basal sliding velocity (u_b) is proportional to the basal drag (τ_b) to the third power:

$$245 \quad u_b = -A_{sl}\tau_b^3 \quad (6)$$

The basal drag corresponds to the sum of all basal resistive stresses. A_{sl} is the sliding parameter which is defined as a constant in the model and calibrated for every specific ice mass (see section 3.3). There is no basal sliding when the basal ice temperature is below the pressure melting point. The ice temperatures are calculated at all timesteps and for every location using the
250 approach of Van Tricht and Huybrechts (2022). The parameters for warming due to refreezing and snow insulation found in their study are considered to be constant in space and time for the different ice masses.

The model is run on a 25 m resolution with 21 layers in the vertical, spaced more closely towards the bottom. Calibration consists of tuning the enhancement factor and the basal sliding parameter to minimise differences between modelled and
255 observed ice thickness. The ice flow model is coupled to a simplified surface energy balance model that calculates the spatio-temporal distribution of the surface mass balance (see section 3.2). The continuity equation (Eq. 7) is used to link both models:

$$\frac{\partial H}{\partial t} = -\nabla(\bar{u}H) + m_s \quad (7)$$

260 With H the ice thickness, \bar{u} the vertically average horizontal velocity vector, ∇ the 2-d divergence operator and m_s the surface mass balance. The higher-order velocity field and the changes in ice thickness are calculated twice a week, while the surface mass balance is updated annually.

3.2 Surface mass balance model

265 The selected surface mass balance model is the simplified energy balance model that has been optimised, calibrated, and used in Van Tricht et al. (2021b) for different glaciers in the Tien Shan. The model is based on the net energy balance at the surface with incoming solar radiation, albedo and transmissivity, as well as two tuning parameters (C_0 and C_1) representing the sum of the net longwave radiation balance and the turbulent sensible heat exchange. A recent representation of the surface elevation
270 is used to calculate the insolation based on local slope and aspect, shadow and the elevation-dependent temperature and precipitation.



Calibration of the model is carried out based on measured mass balances at stakes which are interpolated to average values for elevation bands of 100 metres. The input data of the surface mass balance model is limited to hourly precipitation and temperature data of meteorological stations in the vicinity of the ice masses and a recent surface DEM. An overview of the most important parameters of the surface mass balance model is given in Table 2. C_1 is kept fixed at 24 as was found in Van Tricht et al. (2021a). C_0 is initially taken from Van Tricht et al. (2021b) and Van Tricht and Huybrechts (2022), and then further adjusted based on mass balance observations of the 2020/21 season. All other parameters are reproduced from Van Tricht et al. (2021b). A sinusoidal course of the lapse rate (vertical temperature gradient) is created, based on the monthly lapse rates provided by Aizen et al. (1995), to ensure a smooth transition during the year (see Table 3). To correctly reproduce the surface layer temperatures, needed to model the englacial temperatures, the amount of refrozen water and the maximum snow thickness in May are estimated, following the approach described in Van Tricht and Huybrechts (2022).

Table 3: Overview of the calibrated parameters. For some ice masses, two different precipitation gradients are adopted, indicated by the subscript 1 and 2, to account for moisture depletion in the upper reaches. h_{crit} is the elevation (m a.s.l.) above which the second precipitation gradient is used.

	Ashu-Tor	Bordu	Golubin	Grigoriev	Kara-Batkak	Sary-Tor
C_1	24	24	24	24	24	24
C_0	-195	-191	-228	-195	-193	-192
$\partial P / \partial z_1$ [m w.e. km ⁻¹]	0.70	0.50	0.20	0.15	0.30	0.50
h_{crit}	/	4400	4050	/	4200	4400
$\partial P / \partial z_2$ [m w.e. km ⁻¹]	/	-0.40	-1.50	/	-4.00	-0.40
$\partial T / \partial z$ [°C km ⁻¹]	Sinusoidal with a minimum of -6.2 in June and a maximum of -2.3 in December For the Golubin glacier, sinusoidal with a minimum of -7.4 in June and a maximum of -3.5 in December					

3.3 Calibration of the flow parameters

Our initial iterative minimisation procedure aims to simulate the ice thickness distribution as close as possible to the observations. The observations concern the ice thickness distribution of the different ice masses created from measurements and modelling for the Ashu-Tor, Bordu, Kara-Batkak and Golubin glaciers (Van Tricht et al., 2021a), the Grigoriev ice cap (Van Tricht and Huybrechts, 2022), and the Sary-Tor glacier (Petraikov et al., 2014) (see Table 1). To do this, the coupled velocity and temperature fields are run forward until a steady state is reached using average 1960-1990 climatic conditions. The latter period is considered as the climate regime resulting in the present-day ice geometry, considering a typical response time of 30-60 years. To take into account a mismatch of the steady state assumption, the surface mass balance distribution is homogeneously adjusted to optimally fit the modelled extent of the ice masses with the ice mass extent of the observations (length calibration).



When a steady state is reached (zero ice thickness change), the obtained ice thickness distribution is compared with the measured ice thickness distribution and the RMSE is calculated. Subsequently, the basal sliding parameter (A_{sl}) and the enhancement factor (m) are adjusted, and the model is run until a new steady state is reached for the new parameter combination. Calibration then consists of looking for the combination of parameters with a minimal RMSE between modelled and observed ice thickness. The enhancement factor is varied between 1 and 15 in steps of 1 and the basal sliding parameter is varied between 5×10^{-15} and $1 \times 10^{-13} \text{ m}^8 \text{ N}^{-3} \text{ yr}^{-1}$. The parameter combination with the minimum RMSE for every ice mass is used for the initial runs. In the dynamical calibration procedure (see section 4.2), the flow parameters might be further adjusted by comparing time-dependent modelled ice thickness and velocities (if available) with observations.

310 **Table 4:** Calibration of the flow parameters

	Ashu-Tor	Bordu	Golubin	Grigoriev	Kara-Batkak	Sary-Tor
Enhancement (m)	2	2	3	2	4	3
Basal sliding (A_{sl}) ($\text{m}^8 \text{ N}^{-3} \text{ yr}^{-1}$)	5×10^{-14}	5×10^{-14}	5×10^{-14}	5×10^{-14}	1×10^{-14}	5×10^{-14}
RMSE ice thickness (m i.e.)	11.7	16.8	11.2	14.1	12.8	16.1
RMSE velocity (m yr^{-1}) (nr. Obs.)	2.6 (7)	1.8 (24)	1.8 (15)	0.3 (8)	11.0	1.7 (43)

The optimal enhancement factors and basal sliding parameters are close to each other (Table 4), which increases the confidence in the calibrated values, and which shows that these patterns might be regionally uniform. The RMSE between modelled and measured ice thickness is for all ice masses between 11 and 17 m, while the ME is between -4.6 m and 11.8 m. With average ice thicknesses of about 100 m, this shows that the modelled ice thicknesses are within 10% of the observations. The RMSE of the modelled velocities are of the order of 1-3 m yr^{-1} , except for the Kara-Batkak glacier for which the RMSE is larger (11 m yr^{-1}). With regard to the latter, the velocities are much higher (up to 60 m yr^{-1}) and for the highest values there are some mismatches that strongly affect the RMSE (see Figure 6). For the comparison between modelled velocities and observed velocities of the Grigoriev ice cap, we use the stake locations of Fujita et al. (2011) from 2006-2007. It must be noted that these were only located in the upper (and slower) part of the ice cap. One additional velocity observation could be created based on feature tracking on the eastern outlet glacier using Sentinel satellite images of 2017 and 2018.

3.4 Geometric data

The input data of the ice flow model is limited to a bedrock DEM which is determined by subtracting the measured and reconstructed ice thickness of the different ice masses (Petraikov et al., 2014; Van Tricht et al., 2021a; Van Tricht and Huybrechts, 2022) from a surface DEM as close as possible to the date of the ice thickness data. To represent the surface elevation, the TerraSAR-X add-on for Digital Elevation Measurement mission (TanDEM-X) (2013) is selected. In the frontal areas for all glaciers, and for the entire Bordu glacier, Grigoriev ice cap and Sary-Tor glacier, the surface DEM is derived from



photogrammetrically created Digital Surface Models (DSMs) from UAV images in 2021, created following the approach described in Van Tricht et al., 2021c. A LIA mask is created to avoid ice flowing over ridges away from the glaciers in the accumulation areas. This mask is determined by manual delineation of the LIA ice boundary based on unique and well-recognisable moraines on satellite images from Sentinel and Landsat. The LIA extent and the retreat of the Golubin glacier is adopted from data presented in Aizen et al. (2006), which date back to tacheometric surveys from the mid 19th century (Venukov, 1861). In 1861, the Golubin glacier terminus was located in a deep canyon at 2900 m a.s.l. (Venukov, 1861; Aizen et al., 2006). Between 1861-1913, the terminus retreated to 3050 m a.s.l. From 1913 to 1949, the terminus retreated to an elevation of 3150 m and by 1963, it reached 3250 m a.s.l. Between 1958 and 1982, small annual oscillations of the terminus position were measured (Aizen et al., 1983). From 1982 onwards, the terminus retreated in a rather constant way.

340

4 Dynamical calibration and historical reconstruction

To obtain a reliable prognosis of the future evolution of the selected ice masses, it is crucial to simulate their historical retreat, because the current ice masses are still responding to past changes. Therefore, the ice flow model is first dynamically calibrated to reproduce the observed retreat since the end of the LIA. For this purpose, outlines of different years, which are derived from satellite images (Landsat, Sentinel) and from previous reconstructions, are used.

345

4.1 Ice geometry at the end of the LIA

The starting point of the historical reconstructions is the end of the LIA which is set at 1850, based on obtained lichenometric dates of LIA moraines (Savoskul and Solomina, 1996; Solomina et al., 2004; Li et al., 2017). To start, the coupled model is run for constant average 1820-1850 climatic conditions until a steady state is reached. Then, the obtained ice masses are compared with the LIA extent derived from clearly visible unique end moraines on satellite images. Based on this comparison, a uniform mass balance bias is searched and applied to acquire the LIA geometry of all ice masses (Table 5). The small bias needed to reconstruct the LIA (-0.20 to +0.04 m w.e.) shows a rather good reliability of the meteorological data used to represent the end of the LIA.

355

Table 5: Reconstructed ice volume and maximum ice thickness at the end of the Little Ice Age of the different ice masses. A mass balance bias is added to acquire the supposed LIA extent.

360

	Ashu-Tor	Bordu	Golubin	Grigoriev	Kara-Batkak	Sary-Tor
Ice volume (km³)	0.66	0.61	0.45	0.71	0.20	0.28
Max ice thickness (m)	214	189	186	115	164	177
m_s bias (m w.e. yr⁻¹)	-0.20	+0.04	+0.03	-0.20	+0.04	0



The geometry of the LIA of the different ice masses resulting from the calibrated ice flow model is significantly larger than the present-day outline, especially in the frontal areas (Figure 3). Higher up the ice masses, at the altitude of the current accumulation areas, the ice geometry has changed little, both in thickness and in extent. The Bordu and Sary-Tor glaciers, which are located in neighbouring valleys, have a gently sloping bedrock so they had very similar thicknesses and sizes at the end of the LIA. The Ashu-Tor glacier is situated on a flat bedrock, which characterises this glacier by a distinctly thicker ice body. The Kara-Batkak glacier occupies a much greater elevation interval and has a steeper bedrock. Therefore, this glacier has always been thinner compared to the other ice masses. However, at the end of the LIA, the maximum ice thickness was 30% more than the current maximum. The Golubin glacier extended at the end of the LIA much more to the northwest ending at a steep north facing valley side (Venukov, 1861). The Grigoriev ice cap was especially larger at the southern margin and also merged with the Chontor glacier to the west and the Popova glacier to the east (both are not modelled in this study).

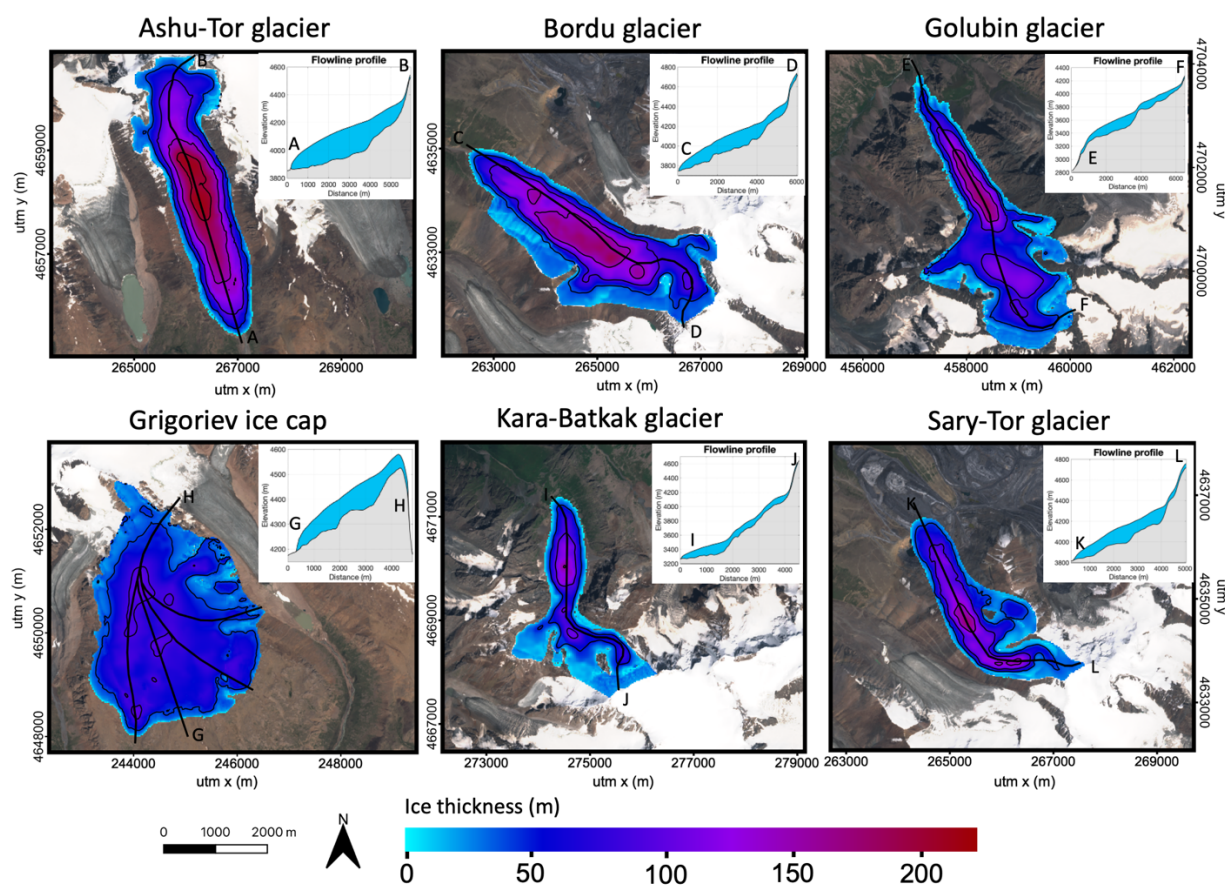


Figure 3: LIA geometries of the different ice masses, reconstructed with the ice flow model and 1820-1850 climatic conditions. The inset shows the bedrock and surface profile along the main flowline, indicated with a black line. The background satellite images are from Sentinel-2 data.



4.2 Ice evolution between 1850 and 2021

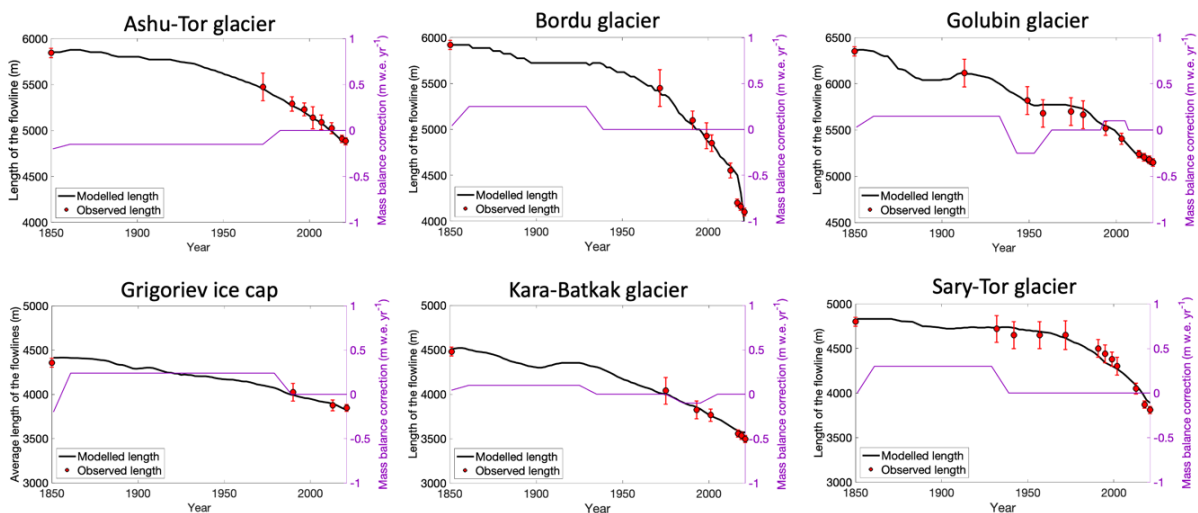
380

Then, starting from the obtained steady state LIA geometry (Figure 3), the surface mass balance is annually calculated using the energy balance model to simulate the historical evolution of the ice masses between 1850 and 2021. The modelled length of the central flowline is compared with lengths derived from satellite data. Since the Grigoriev ice cap does not have a unique central flowline, as is typical for an ice cap, we chose to use 4 separate flowlines and dynamically calibrated for the mean
 385 length of the flowlines. By comparing with the intermediate extents, a uniform mass balance bias (δm_s) is searched and iteratively added (Eq. 8) to match the historical modelled extents optimally with the observed extents, similar to the approach of Zekollari et al. (2014).

$$m_s(x,y,t) = m_s(x,y,t) + \delta m_s \quad (8)$$

390

This bias implicitly accounts for uncertainties in the mass balance model and errors in the climatic records. The bias varies in time and appears to be necessary to reproduce closely the observed retreat of the different ice masses. For at least the last three decades, which corresponds to a typical response time of the studied ice masses (Jóhannesson et al., 1989), no biases need to be applied to correctly reconstruct the observed retreat. This suggests that the surface mass balance derived for the recent
 395 (more accurate data from local measurements) decades provides a more correct forcing for the ice flow model, which increases the confidence in the calibrated model used in this study.



400 **Figure 4:** Reconstructed retreat of the different ice masses along the main flowline and observed extent (red circles). The surface mass balance bias is shown as the purple line. The red dots represent the observed length. The confidence interval (red whiskers) is determined based on the quality and the resolution of the satellite data used for the determination of the front positions.



In the second half of the 19th century, the ice masses only slightly retreated (Figure 4). Then, in the beginning of the 20th century, lower temperatures ensured for some of the ice masses a period of (slight) advance, which is most noticeable for the Golubin glacier and the Kara-Batkak glacier, which are characterised by the smallest response time following the approach of Jóhannesson et al. (1989). In the second half of the 20th century and especially after 1970, the retreat clearly accelerated for all of the ice masses.

4.3 Comparison with observed ice thicknesses and surface velocities

410

A first validation of the ice flow model and the dynamical calibration is performed by comparing the obtained ice thickness with measured ice thickness (Petraikov et al., 2014; Van Tricht et al., 2021a; Van Tricht and Huybrechts, 2022), and by comparing with surface velocities. There is clearly a good correspondence between the modelled thickness and the measured and reconstructed thickness with in general small differences, especially for the areas where GPR measurements were made.

415 We find overall a low RMSE and mean error (ME) (Figure 5). This increases the confidence in the model parameters selected in this study.

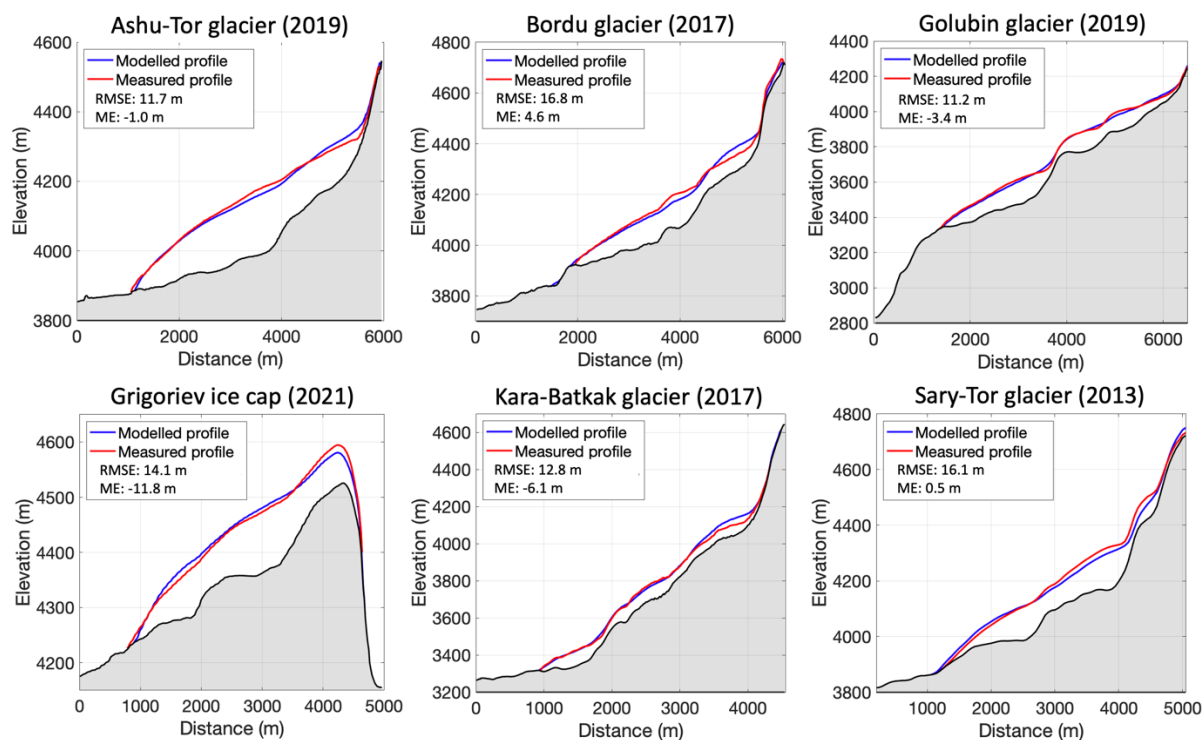


Figure 5: Validation of the modelled ice thickness profile with measured and reconstructed ice thicknesses.



420

A second validation is performed by comparing modelled surface velocities with point surface velocities derived from stake displacements and displacements of features such as well-detectable supraglacial boulders on the UAV images and satellite images. Like for the ice thickness, we find a close agreement with low values of the RMSE and the ME. In addition, there does not seem to be a bias towards higher or lower velocities for any of the ice masses compared to the observations.

425

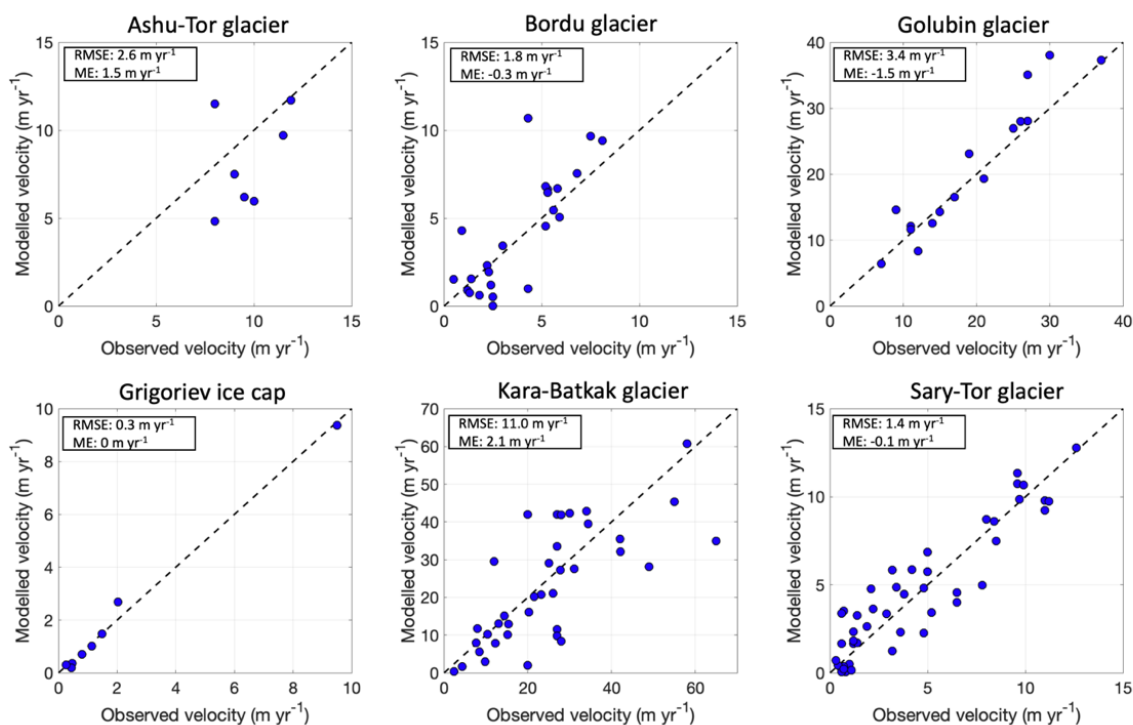


Figure 6: Validation of the modelled surface velocities with measured velocities.

5 Future evolution of the ice masses

430

5.1 Projected ice volume and area for 2022-2100

Under all considered SSP-scenarios, the results show a strong volume and area loss for all ice masses (Figure 7). In the case of the SSP5-8.5 scenario, the ice masses entirely disappear by 2100, except for the Kara-Batkak glacier for which 10% of the 2021 volume remains, located in the upper area (Figure 9). The rate of decline of the ice masses varies, although the majority of the ice masses already disappear by 2080.

435



For the other SSP-scenarios, there are some notable differences in response of the ice masses to the imposed climate. The Grigoriev ice cap retreats under all climate scenarios to (almost) 0% of its current volume (Figure 7). Even under the 2001-
440 2021 climate, only 40% of the present-day ice volume remains by 2100. This very strong retreat of the Grigoriev ice cap can be explained by the limited altitudinal extent and the ‘small ice cap instability’. The Grigoriev ice cap is located on top of a rather flat mountain which means that the ice cap cannot retreat to higher elevations (Van Tricht and Huybrechts, 2022). At present, the ELA is located around 4350-4400 metres which is only 100-150 metres below the summit. A more negative mass balance in the future causes a thinning and a lowering of the surface, which amplifies the melting (positive feedback effect).
445 The Grigoriev ice cap is therefore largely dependent on its own height to sustain itself, while glaciers can migrate up- or downwards when reacting to a changing climate. Under SSP2-4.5, the ELA already rises to the summit before the middle of the 21st century (Figure 8).

The evolution of the Ashu-Tor, Bordu and Sary-Tor glaciers is under all scenarios rather similar (Figure 7). Under the present-
450 day climate, about 50% of the current volume remains in 2100. Under SSP1-1.9 and SSP1-2.6, most of the ice mass disappears except for the upper areas, with a total remaining volume which is about 10-30% of the current volume. Under SSP2-4.5 and SSP3-7.0, the glaciers disappear (almost) completely, except for some smaller patches at the highest elevations, which would likely also melt after 2100. Figure 8 reveals that under SSP2-4.5, the ELA rises to the highest elevations of the Ashu-Tor glacier by 2050, and slightly later for the Bordu and the Sary-Tor glaciers.

455 The Kara-Batkak glacier is the one with the largest percentage of volume remaining in any scenario (Figure 7). This can be explained by a combination of the large altitudinal range (which means that the glacier can migrate to higher altitudes), and the larger amount of winter and spring precipitation for this glacier. The latter makes the accumulation less sensitive to temperature changes compared to the glaciers in the drier area of the Inner Tien Shan, which are mainly characterised by spring
460 and (early) summer accumulation. This is also clear from Figure 8 which displays that under the SSP2-4.5 scenario, more than 50% of the glacier area is located in the accumulation area by 2100.

Regarding the Golubin glacier, we find a large difference between the SSP1-1.9, SSP1-2.6, and SSP2-4.5 scenarios (Figure 7). This is related to the specific geometry. The Golubin glacier consists of a large plateau that under SSP2-4.5 is located below
465 the ELA while under SSP1-2.6, in 2100, it is still around the ELA and under SSP1-1.9, it is still located above the ELA. This underscores the fact that in order to understand the response of an ice mass to climate change, and to compare it with other ice masses, the specific geometry has to be considered.

470

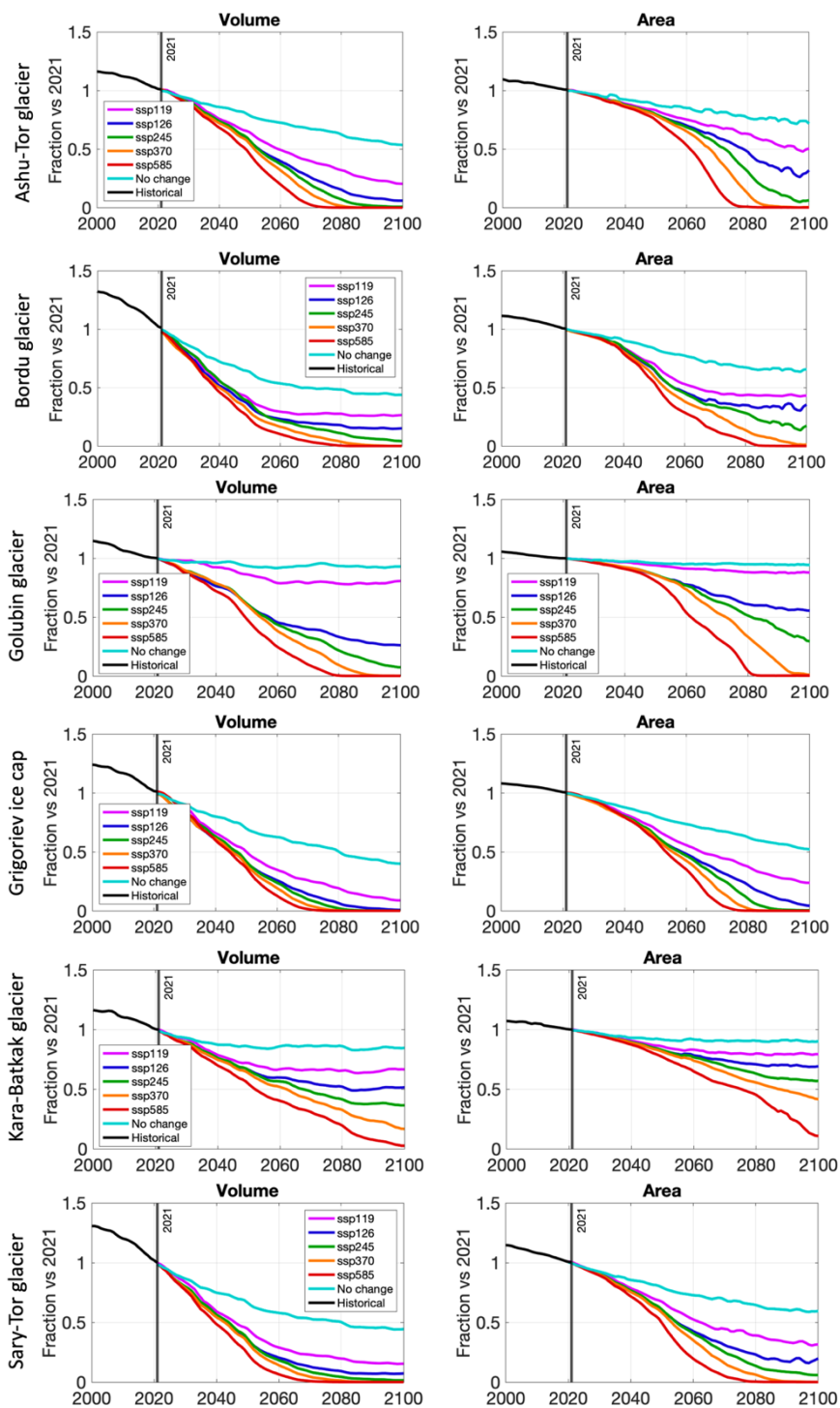


Figure 7: Historical and future evolution of the ice volume and area with respect to 2021 for the different ice bodies.



475

In the case of a constant 2001-2021 mean climate, the Ashu-Tor, Bordu and Sary-Tor glaciers as well as the Grigoriev ice cap retreat strongly with a volume of 40-50% of the present-day volume remaining by 2100 (Figure 7). This shows the current imbalance of these ice masses with a large, committed ice loss. The loss of the Golubin and the Kara-Batkak glacier under the 2001-2021 climate is much lower which means that these ice masses currently have a volume and area that is more in balance with the current climatic conditions.

480

The strong sensitivity of the studied ice masses to climate change can be explained by the specific climate regime. The ice masses in the Tien Shan are spring-summer accumulation type of glaciers (Aizen et al., 2006; Fujita, 2008; Van Tricht et al., 2021b), which means that the accumulation is more sensitive to temperature changes. The air temperature in spring and summer both affects the duration and intensity of melt as well as the type of precipitation, in contrast to glaciers and ice caps with accumulation centred on winter, for which temperatures remain (to date) low enough for solid precipitation. This ensures that warming on winter-type glaciers mainly prolongs and intensifies the melting period without significantly changing accumulation and the average albedo (Aizen et al., 2006; Fujita, 2008). Next to that, in the Tien Shan, the episodic solid precipitation events between May and September preserve the ice from intense melting by increasing the surface albedo which interrupts the melting season temporarily (Che et al., 2019; Van Tricht et al., 2021b). However, increasing temperatures in spring and summer increase melting and reduce the surface albedo as more precipitation falls in liquid state.

485

490

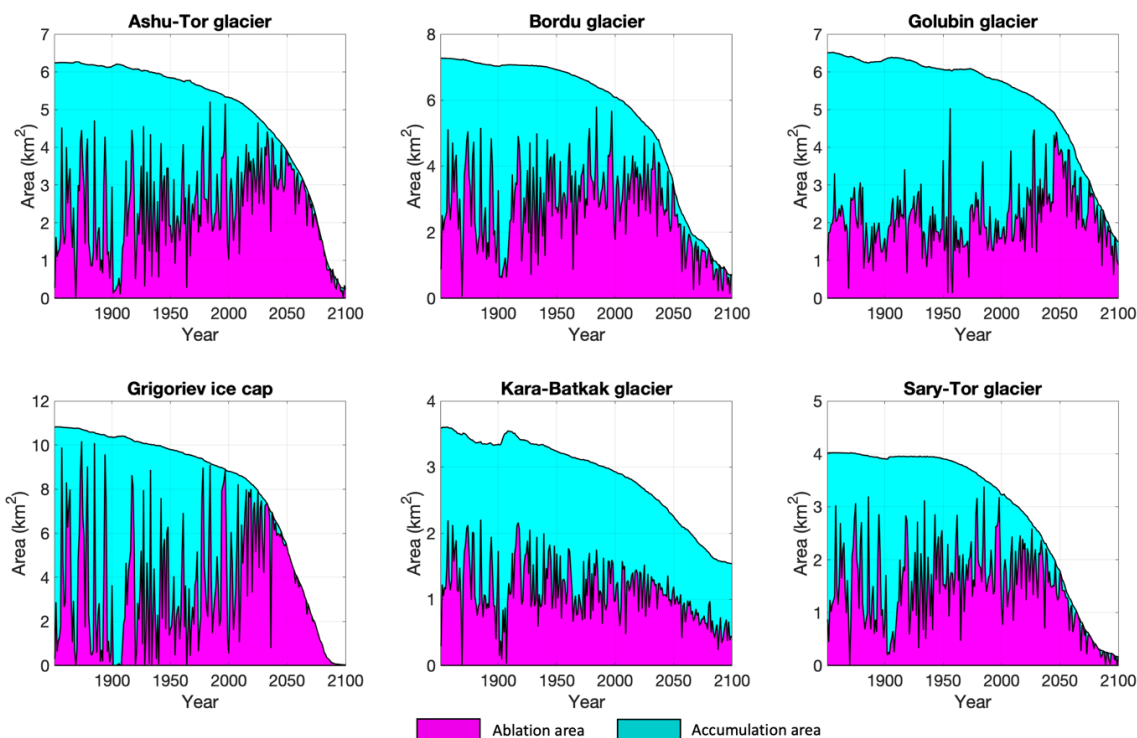


Figure 8: Evolution of the accumulation area and the ablation area under SSP2-4.5 for the different ice masses.

495

5.2 Ice masses in 2100

The ice masses in 2100 are clearly smaller than the present-day geometries in all scenarios (Figure 9). Nevertheless, it is clear that, depending on the scenario, more or less ice will remain by the end of the 21st century. For the optimistic SSP1-1.9 and 500 SSP1-2.6 scenarios, most ice masses maintain (individual) patches of ice in the upper areas, except for the Grigoriev ice cap which collapses (almost) completely. After the retreat of the ice, the bedrock will appear.

As the 2-d profiles in the inset already show, there are several (small) depressions in the bedrock that have been scoured by years of ice erosion (Figure 9). In these bedrock depressions, which will eventually become free of ice, it is very likely that 505 (proglacial) lakes will form (Furian et al., 2022; Compagno et al., 2022). Their formation might accelerate frontal retreat by hydrostatic lifting of the frontal area (Carrivick et al., 2020).

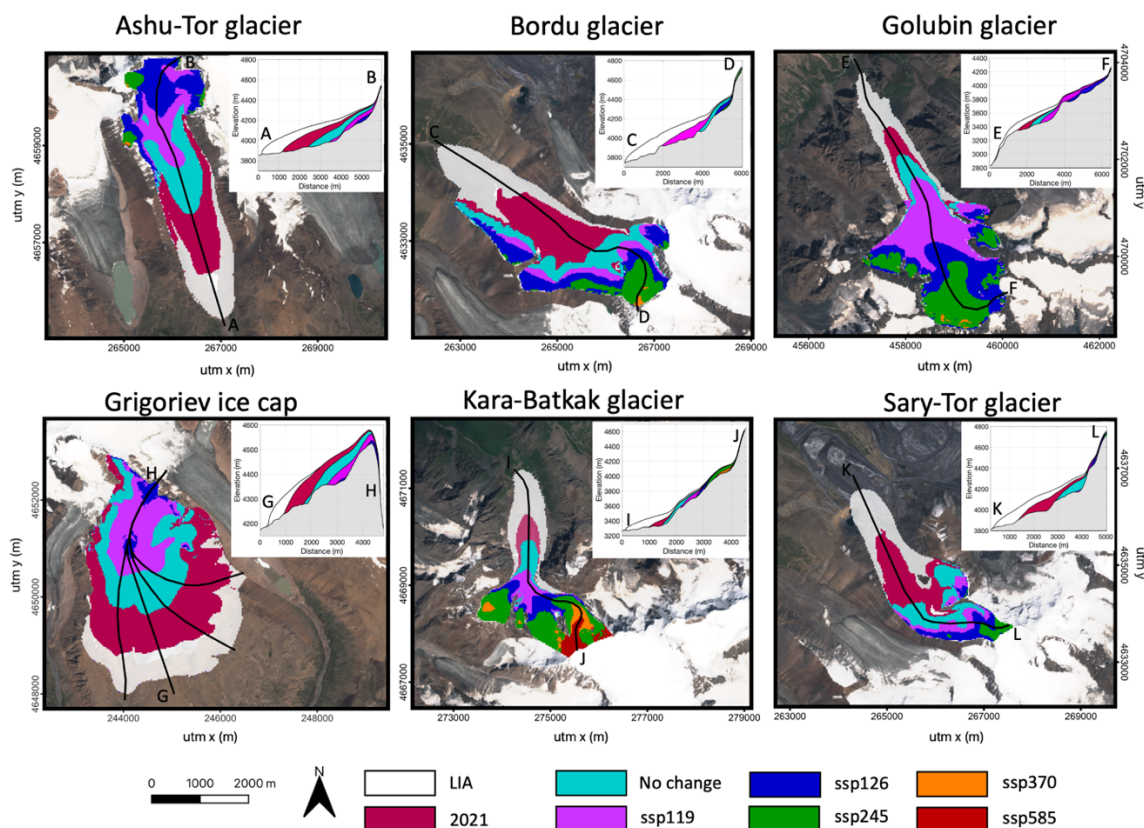


Figure 9: Extent of the ice masses at the end of the Little Ice Age (LIA), in 2021 and in 2100 under different climatic scenarios. The inset shows the bedrock and surface profile along the main flowlines indicated by the black lines on the respective maps. The background satellite images are from Sentinel-2 data.

5.3 Runoff

The melting of the ice masses in the Tien Shan, which will accelerate in the coming decades (Figure 7) will lead to profound changes in the runoff. To analyse the projected evolution in the runoff originating from the different ice masses, the annual total runoff is calculated following the approach of Huss and Hock (2018) and Rounce et al. (2019). The runoff (r_{tot}) is defined as all water that leaves the initial (LIA) glacierised area in one year. This is computed from the difference between the total precipitation (P_{tot}) and the mass balance within that area. As such, in the ablation area, the total runoff is the sum of the total precipitation and the glacier meltwater. In the accumulation area and outside the ice masses, it is equal to the total precipitation minus the snow/refrozen water present at the end of the year. Defining the runoff as in Eq. 9 is equivalent to the runoff that would be measured at a fixed gauge at the LIA glacier terminus (Rounce et al., 2019).

$$r_{\text{tot}} = \sum_{x,y} (P_{\text{tot},[x,y]} - m_{s,[x,y]}) \quad (9)$$

525

The results show that after an initial increase in the total annual runoff, the continuous retreat of the ice masses leads to a significant decrease in runoff during the second half of the 21st century (Figure 10). A peak in the total runoff is expected to be reached before 2050 in all scenarios. Higher SSP-scenarios clearly have a higher peak due to the increased excess glacier meltwater, which corresponds to the additional runoff due to annual glacier net mass loss. However, this peak is shorter, occurs earlier, and a drastic decrease in total runoff follows afterwards.

530

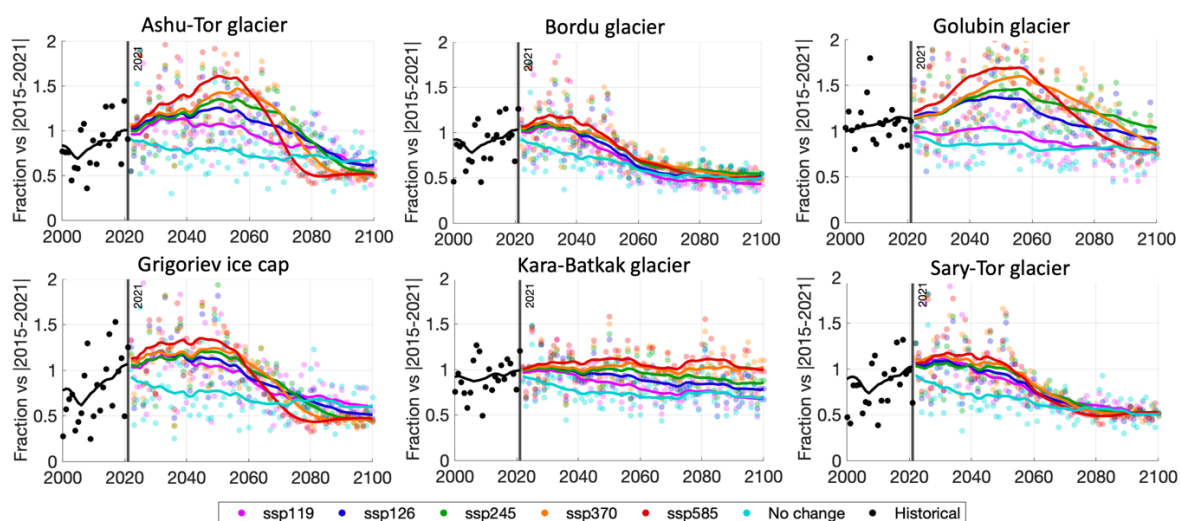


Figure 10: Annual total runoff from the initially (Little Ice Age) glacierised area under different climate scenarios. The points represent the modelled total runoff in every year while the solid line is 10 year moving average.

535

Compared to the 2015-2021 average, the total runoff is shown to be reduced on average by 50% by the end of the 21st century in all scenarios, except for the Golubin and the Kara-Batkak glaciers for which the total runoff remains larger (Figure 10). It is beyond the focus of this study, but the timing and intensity of runoff during the year also changes, with the peak runoff occurring earlier in the year (Rounce et al., 2019). This is because glacial meltwater is a more gradual source of runoff during spring and summer, while runoff from rain/snow is more intense and temporary. During the 21st century, the proportion of ice melt decreases as the ice masses all become significantly smaller in all scenarios. Therefore, the glacial-nival regimes in the region will eventually transform into nival-pluvial regimes with larger year-to-year variability (Braun and Hagg, 2009; Sorg et al., 2013).

545



6 Discussion and outlook

550 6.1 Uncertainty and limitations

The applied methods and the obtained results comprise several uncertainties and limitations which need to be noted. For the future projections, a multi-model mean was created based on all available GCMs covering the study area. To do this, anomalies with respect to overlapping periods between the GCMs and observations were used and transposed to the future. Although a multi-model mean is beneficial because biases in individual models are less prominent, the use of regional climate models such as CORDEX, or downscaled products, might show additional smaller scale details and variations (Rana et al., 2020). These small-scale variations, which depend on local elevation and topography, are not included in the forcing of the future but might influence the evolution of the studied ice masses. Nevertheless, a recent study considering glacier evolution in Iceland and Scandinavia pointed out that climate forcing products were only of minor importance for future glacier projections, as opposed to accurate model calibration data at the glacier-specific scale (Compagno et al., 2021).

Regarding the englacial temperatures, it must be stated that we used the same constants for the snow insulation and firn warming to parametrise the surface layer warming as derived in Van Tricht and Huybrechts, (2022). However, these constants were only calibrated based on ice temperature data of the Grigoriev ice cap. Nevertheless, validation with GPR-measurements showed a close match for Sary-Tor glacier as well, which increases our confidence that the derived values can be transferred to other glaciers in the region as well. It must also be stated that the mass balance model of the Ashu-Tor glacier is strongly based on the calibrated parameters of nearby glaciers, as direct mass balance measurements were only performed for a limited period in time and for a limited altitudinal extent. We specifically want to highlight that given the highly variable precipitation gradient, which is for example evident from the difference of the precipitation gradient between the Bordu glacier and the Grigoriev ice cap, modelled mass balances in the accumulation area of this glacier are characterised by a larger uncertainty.

6.2 Comparison with geodetic mass balances

As an individual and independent validation of our study, the historical reconstructions of the ice masses are compared with geodetic mass balances for multiple periods (Table 6). In general, we find a close correspondence that is mostly within the uncertainty ranges of the geodetic mass balances. Only for the Kara-Batkak glacier, there are larger discrepancies which might be caused by the absence of the highest part of the accumulation area in the RGI version 6.0 dataset that is used to derive most of the geodetic mass balances. For the latest dataset, which comprises the elevation change rate of 2000-2019 (Hugonnet et al., 2021), we find for all ice masses a very close correspondence, except for the Ashu-Tor glacier (Table 6). The geodetic



580 value for this glacier seems to be very negative and much lower than for the surrounding glaciers. The Kara-Batkak glacier is clearly characterised by the least negative modelled elevation change rate as geodetic mass balance (Table 6), which matches to the slower and more limited retreat and melting of this glacier (see also Figure 7).

585 **Table 6:** Comparison between geodetic mass balances and modelled elevation change rates for different periods. Both values are given in m w.e. yr⁻¹.

	Ashu-Tor glacier		Bordu glacier		Golubin glacier	
	Geodetic	Modelled	Geodetic	Modelled	Geodetic	Modelled
1964-1999 ¹					-0.46 ± 0.24	-0.12
1975-1999 ²			-0.79 ± 0.25	-0.64		
1999-2012 ¹					-0.28 ± 0.97	-0.31
2006-2014 ³					-0.30 ± 0.37	-0.41
2000-2016 ⁴	-0.55 ± 0.22	-0.36	-0.43 ± 0.17	-0.46	-0.05 ± 0.22	-0.34
2000-2018 ⁵	-0.57 ± 0.11	-0.38	-0.35 ± 0.11	-0.48	0.09 ± 0.31	-0.33
2000-2019 ⁶	-0.87 ± 0.16	-0.40	-0.50 ± 0.15	-0.48	-0.30 ± 0.16	-0.31
	Grigoriev ice cap		Kara-Batkak glacier		Sary-Tor glacier	
	Geodetic	Modelled	Geodetic	Modelled	Geodetic	Modelled
1943-1977 ⁷					-0.48	-0.30
1964-1980 ⁸					-0.30 ± 0.40	-0.38
1975-1999 ²			-0.54 ± 0.25	-0.25	-0.51 ± 0.25	-0.51
2000-2016 ⁴			-0.45 ± 0.03	-0.17	-0.45 ± 0.23	-0.37
2000-2018 ⁵			-0.19 ± 0.14	-0.18	-0.43 ± 0.18	-0.39
2000-2019 ⁶	-0.34 ± 0.16	-0.42	-0.16 ± 0.34	-0.20	-0.48 ± 0.16	-0.40

¹Bolch et al., (2015); ²Pieczonka and Bolch, (2015); ³Barandun et al., (2018); ⁴Brun et al., (2017); ⁵Shean et al., (2020); Hugonnet et al., (2021); ⁷Aizen et al., (2007); ⁸Goerlich et al. (2017)

590 7 Conclusion

In this study, we modelled the historical and future evolution of six ice masses in the western part of the Tien Shan mountains, High Mountain Asia, using a 3-dimensional higher-order ice flow model coupled to a surface energy mass balance model. The models were calibrated with surface mass balance measurements, length reconstructions and ice thickness data. Data from tree rings and weather stations in the vicinity of the ice masses served as meteorological input data for the past. For the Golubin glacier, precipitation data of ERA5 were used as well. Subsequently, different CMIP6 SSP scenarios were considered for the future projections up to 2100 as well as a no change scenario keeping the average climatic conditions of 2001-2021 constant.



Using small mass balance adjustments accounting for uncertainties in the mass balance model and errors in the climatic records, the historical retreat of the ice masses between the Little Ice Age and 2021 could be closely reproduced. Validations with present day observations showed a close correspondence. The results show a clear increase of the retreat of the ice masses in recent decades.

The projections of the ice masses up to 2100 reveal that under all climate scenarios, the ice masses become significantly smaller. Under the SSP5-8.5 scenario, most of the ice masses disappear altogether, except for the Kara-Batkak glacier which appears to be able to maintain small ice patches at the highest elevations. The Grigoriev ice cap shows the strongest climate sensitivity, disappearing in almost every climate scenario. This could be explained by the small ice cap instability, with the equilibrium line rising above the top of the ice cap even in the most optimal climate scenario. Besides, the studied ice masses appear to be particularly sensitive to climate change because the accumulation is centred on spring and early summer. Hence, temperature rises in these seasons do not only amplify melting but also reduce the solid part of the precipitation and the average albedo. Projections of the total annual runoff from the LIA glacierised catchment show that the peak water will be reached before the mid of the 21th century and that the intensity of this peak depends on the climate scenario, with a higher warming scenario having a larger peak.

The availability of a comprehensive set of accurate direct measurements allowed us to study in detail a sample of six ice masses in the Tien Shan. The different geometries and climatic settings of the ice bodies additionally permitted analysis of why certain ice masses disappear faster (e.g. the Grigoriev ice cap) or can survive (e.g. the Kara-Batkak glacier). In a next step, it would be interesting to compare the results of this study to the outcomes of simpler regional models providing ice volume evolutions for all glaciers in the study area. This can give an inside in the added-value of using higher-order models and it will allow to assess the value and quality of larger-scale models that are required for regional studies of ice volume evolution.

620

8 Code availability

Information and specific details about the model code will be specified on request by Lander Van Tricht.

625 9 Author contributions

LVT collected the input data, prepared the climate scenarios, performed the experiments, and wrote the manuscript. PH provided the model code and gave guidance in implementing the research and interpreting the results, assisting during the entire process.

630



10 Competing interests

635 The contact author has declared that none of the authors has any competing interests.

11 Acknowledgements

640 The authors would like to thank everyone who contributed to the fieldwork to carry out the ice thickness measurements and the drone surveys. We would also like to specifically thank Oleg Rybak and Rysbek Satylkanov for assisting and organising the fieldwork. We thank Victor Popovnin for providing mass balance data. We are also grateful to the Kumtor Gold Mine for allowing us to perform glacier measurements on their concession.

12 Financial support

645

Lander Van Tricht holds a PhD fellowship of the Research Foundation – Flanders (FWO-Vlaanderen) and is affiliated with the Vrije Universiteit Brussel (VUB). Logistics for fieldwork on the glaciers were mainly organised and funded by the Tien Shan High Mountain Research Center and the Kumtor mining company.

650 13 References

Aizen, V.B., Maksimov, N.V. and Solodov, P.A.: Dynamicalednika Grolubina za poslednie 20 let [Dynamic of the Golubina Glacier for the 20 last years]. Trudi Central'no-Asiatskogo Regional'nogo Nauchno-Issledovatel'skogo Instituta [Works of Central Asian Regional Institute of Science Investigations, Tashkent], 91(172), 1983

655

Aizen, V. B., Aizen, E. M., and Melack, J. M.: Climate, Snow Cover, Glaciers, and Runoff in the Tien Shan, Central Asia, J. Am. Water Resour. As., 31, 1113–1129, <https://doi.org/10.1111/j.1752-1688.1995.tb03426.x>, 1995.

660 Aizen, V. B., Kuzmichenok, V., Surazakov, A., and Aizen, E. M.: Glacier changes in the central and northern Tien Shan during the last 140 years based on surface and remote-sensing data, Ann. Glaciol., 43, 202–213, <https://doi.org/10.3189/172756406781812465>, 2006.

Aizen, V.B., Kuzmichenok, V.A., Surazakov, A.B. and Aizen, E.M.: Glacier Changes in the Tien Shan as Determined from Topographic and Remotely Sensed Data. Glob. Planet. Change 56, 328–340.

665 <https://doi.org/10.1016/j.gloplacha.2006.07.016>, 2007



- Arkipov, S. M., Mikhaleiko, V. N., Kunakhovich, M. G., Dikikh, A. N., and Nagornov, O. V.: Termich eskii rezhim, usloviia l'doobrazovaniia i akkumulyatsiia na ladnike Grigor'eva (Tyan'-Shan') v 1962–2001 gg. [Thermal regime, ice types and accumulation in Grigoriev Glacier, Tien Shan, 1962–2001], Mater. Glyatsiol. Issled., 96, 77–83, 2004 (in Russian with English summary).
- 670
- Azisov, E., Hoelzle, M., Vorogushyn, S., Saks, T., Usabaliev, R., Esenaman uulu, M. and Barandun, M.: Reconstructed Centennial Mass Balance Change for Golubin Glacier, Northern Tien Shan. *Atmosphere* 2022, 13, 954.
<https://doi.org/10.3390/atmos13060954>, 2022
- 675
- Barandun, M., Huss, M., Usabaliev, R., Azisov, E., Berthier, E., Kääb, A., Bolch, T., and Hoelzle, M.: Multi-decadal mass balance series of three Kyrgyz glaciers inferred from modelling constrained with repeated snow line observations, *The Cryosphere*, 12, 1899–1919, <https://doi.org/10.5194/tc-12-1899-2018>, 2018.
- 680
- Blomdin, R., Stroeven, A.P., Harbor, J.M., Lifton, N.A., Heyman, J., Gribenski, N., Petrakov, D.A., Caffee, M.W., Ivanov, M.N., Hättestrand, C., Rogozhina, I. and Usabaliev R.: Evaluating the timing of former glacier expansions in the Tian Shan: A key step towards robust spatial correlations. *Quaternary Science Reviews*, 153, 78–96,
<https://doi.org/10.1016/j.quascirev.2016.07.029>, 2016
- 685
- Bolch, T.: Glacier area and mass changes since 1964 in the Ala Archa Valley, Kyrgyz Ala-Too, northern Tien Shan. *Led i Sneg*, 129(01):28–39, <https://doi.org/10.5167/uzh-117189>, 2015
- Braun, L. N. and Hagg, W. Present and future impact of snow cover and glaciers on runoff from mountain regions - comparison between Alps and Tien Shan. *Assess. Snow Glacier Water Resources Asia* 8, 36–43,
690 <https://doi.org/10.5282/ubm/epub.13807>, 2009
- Brun, F., Berthier, E., Wagnon, P., Kääb, A. and Treichler, D.: A spatially resolved estimate of High Mountain Asia glacier mass balances from 2000 to 2016. *Nat. Geosci.* 10, 668–673, <https://doi.org/10.1038/ngeo2999>, 2017
- 695
- Carrivick, J. L., Tweed, F. S., Sutherland, J. L. and Mallalieu, J.: Toward Numerical Modeling of Interactions between Ice-Marginal Proglacial Lakes and Glaciers. *Front. Earth Sci.* 8 (500), 68. <https://doi.org/10.3389/feart.2020.577068>, 2020



- Che, Y., Zhang, M., Li, Z., Wei, Y., Nan, Z., Li, H., Wang, S. and Su, B.: Energy balance model of mass balance and its sensitivity to meteorological variability on Urumqi River Glacier No.1 in the Chinese Tien Shan. *Sci Rep*, 9, 13958, 700 <https://doi.org/10.1038/s41598-019-50398-4>, 2019
- Compagno, L., Zekollari, H., Huss, M. and Farinotti, D.: Limited impact of climate forcing products on future glacier evolution in Scandinavia and Iceland. *Journal of Glaciology*, 67(264), 727-743. <https://doi.org/10.1017/jog.2021.24>, 2021
- 705 Compagno, L., Huss, M., Zekollari, H. and Farinotti, D.: Future growth and decline of high mountain Asia's ice-dammed lakes and associated risk. *Commun Earth Environ* 3, 191, <https://doi.org/10.1038/s43247-022-00520-8>, 2022
- Dikikh, A. N.: Temperature regime of flat-top glaciers (using Grigoriev as an Example) – *Glyatsiol. Issledovaniya na Tyan-Shane*, Frunze, N. 11, 32–35, 1965 (in Russian).
- 710 Dyurgerov, M. B.: Glacier mass balance and regime: data of measurements and analysis, University of Colorado Institute of Arctic and Alpine Research Occasional Paper 55, Boulder, http://instaar.colorado.edu/other/occ_papers.html (last access: 17 October 2022), 2002
- 715 Farinotti, D., Longuevergne, L., Moholdt, G., Duethmann, D., Mölg, T., Bolch, T. and Vorogushyn, S.: Güntner, A. Substantial glacier mass loss in the Tien Shan over the past 50 years. *Nature Geoscience*, 8, 716–722, <https://doi.org/10.1038/ngeo2513>, 2015
- Fujita, K.: Influence of precipitation seasonality on glacier mass balance and its sensitivity to climate change. *Annals of Glaciology*, 48, 88-92. <https://doi.org/10.3189/172756408784700824>, 2008
- 720 Fujita, K., Takeuchi, N., Nikitin, S. A., Surazakov, A. B., Okamoto, S., Aizen, V. B., and Kubota, J.: Favorable climatic regime for maintaining the present-day geometry of the Gregoriev Glacier, Inner Tien Shan, *The Cryosphere*, 5, 539–549, <https://doi.org/10.5194/tc-5-539-2011>, 2011
- 725 Furian, W., Maussion, F. and Schneider, C.: Projected 21st-century glacial lake evolution in High Mountain Asia. *Front. Earth Sci.*, 10, <https://doi.org/10.3389/feart.2022.821798>, 2022
- Fürst, J. J., Rybak, O., Goelzer, H., De Smedt, B., de Groen, P., and Huybrechts, P.: Improved convergence and stability properties in a three-dimensional higher-order ice sheet model, *Geosci. Model Dev.*, 4, 1133–1149, 730 <https://doi.org/10.5194/gmd-4-1133-2011>, 2011



- Fürst, J. J., Goelzer, H., and Huybrechts, P.: Effect of higher-order stress gradients on the centennial mass evolution of the Greenland ice sheet, *The Cryosphere*, 7, 183–199, <https://doi.org/10.5194/tc-7-183-2013>, 2013
- 735
- Gan, R., Luo, L., Zuo, Q. and Sun, L.: Effects of projected climate change on the glacier and runoff generation in the Naryn River Basin, *Central Asia J. Hydrol.*, 523, 240-251, <https://doi.org/10.1016/j.jhydrol.2015.01.057>, 2015
- Goerlich, F., Bolch, T., Mukherjee, K. and Pieczonka, T.: Glacier Mass Loss during the 1960s and 1970s in the Ak-Shirak Range (Kyrgyzstan) from Multiple Stereoscopic Corona and Hexagon Imagery. *Remote Sensing* 9 (3), 275, <https://doi.org/10.3390/rs9030275>, 2017
- 740
- Hagg, W., Braun, L.N., Weber, M. and Becht, M.: Runoff modelling in glacierized central Asian catchments for present-day and future climate. *Hydrology Research*, 37(2), 93–105, <https://doi.org/10.2166/nh.2006.0008>, 2006
- 745
- Hoelzle, M., Azisov, E., Barandun, M., Huss, M., Farinotti, D., Gafurov, A., Hagg, W., Kenzhebaev, R., Kronenberg, M., Machguth, H., Merkulshkin, A., Moldobekov, B., Petrov, M., Saks, T., Salzmann, N., Schöne, T., Tarasov, Y., Usabaliev, R., Vorogushyn, S., Yakovlev, A., and Zemp, M.: Re-establishing glacier monitoring in Kyrgyzstan and Uzbekistan, *Central Asia, Geosci. Instrum. Method. Data Syst.*, 6, 397–418, <https://doi.org/10.5194/gi-6-397-2017>, 2017.
- 750
- Hugonnet, R., McNabb, R., Berthier, E., Menounos, B., Nuth, C., Girod, L., Farinotti, D., Huss, M., Dussaillant, I., Brun, F., and Käab, A.: Accelerated global glacier mass loss in the early twenty-first century. *Nature*, 592, 726-731. <https://doi.org/10.1038/s41586-021-03436-z>, 2021
- 755
- Huss, M. and Hock, R.: Global-scale hydrological response to future glacier mass loss. *Nature Clim Change* 8, 135–140, <https://doi.org/10.1038/s41558-017-0049-x>, 2018
- Hutter, K. (1983). *Theoretical glaciology (Vol. 1)*. Reidel Publ. Co, Dordrecht.
- 760
- Huybrechts, P. A 3-D model for the Antarctic ice sheet: a sensitivity study on the glacial-interglacial contrast. *Climate Dynamics* 5, 79–92, <https://doi.org/10.1007/BF00207423>, 1990
- Kraaijenbrink, P., Bierkens, M., Lutz, A. and Immerzeel W.W.: Impact of a global temperature rise of 1.5 degrees Celsius on Asia's glaciers. *Nature*, 549, 257–260, <https://doi.org/10.1038/nature23878>, 2017
- 765



- Li, Y., Lu, X. and Li, Y.: A Review on the Little Ice Age and Factors to Glacier Changes in the Tian Shan, Central Asia. In book: *Glaciers Evolution in a Changing World* (October). Vienna, Austria: IntechOpen.
<https://doi.org/10.5772/intechopen.70044>, 2017
- 770 Huss, M. and Hock, R.: Global-scale hydrological response to future glacier mass loss. *Nature Climate Change*, *Nature*, 8 (2), 135-140, <https://doi.org/10.1038/s41558-017-0049-x>, 2018
- Immerzeel, W.W., Van Beek, L.P. and Bierkens, M.F.: Climate change will affect the Asian water towers. *Science*, 328, 346-350, <https://doi.org/10.1126/science.1183188>, 2010.
- 775 Jóhannesson, T., Raymond, C. and Waddington, E.: Time-Scale for Adjustment of Glaciers to Changes in Mass Balance. *Journal of Glaciology*, 35(121), 355-369. <https://doi.org/10.3189/S002214300000928X>, 1989
- Jouvet, G., Huss, M., Funk, M., and Blatter, H.: Modelling the retreat of Grosser Aletschgletscher, Switzerland, in a changing climate, *J. Glaciol.*, 57, 1033–1045, <https://doi.org/10.3189/002214311798843359>, 2011
- 780 Mikhailenko, V. N.: Osobennosti massoobmena lednikov ploskikh vershin vnutrennego Tyan'-Shanya [Peculiarities of the mass exchange of flat summit glaciers of interior Tyan'-Shan'], *Materialy Glyatsiologicheskikh Issledovaniy*, 65, 86–92, 1989 (in Russian)
- 785 Narama, C., Daiyrov, M., Duishonakunov, M., Tadono, T., Sato, H., Käab, A., Ukita, J., and Abdrakhmatov, K.: Large drainages from short-lived glacial lakes in the Teskey Range, Tien Shan Mountains, Central Asia. *Natural Hazards and Earth System Sciences*, 18, 983–995, <https://doi.org/10.5194/nhess-18-983-2018>, 2018.
- 790 Pattyn, F.: A new three-dimensional higher-order thermomechanical ice sheet model: Basic sensitivity, ice stream development, and iceflow across subglacial lakes, *J. Geophys. Res.*, 108, B82382, <https://doi.org/10.1029/2002JB002329>, 2003
- 795 Petrakov, D. A., Lavrientiev, I. I., Kovalenko, N. V., and Usabaliev, R. A.: Ice thickness, volume and modern change of the Sary-Tor Glacier area (Ak-Shyirak Massif, Inner Tian Shan), *Earth's Cryosphere*, 18, 91–100, 2014.
- Pieczonka, T. and Bolch, T.: Region-wide Glacier Mass Budgets and Area Changes for the Central Tien Shan between ~1975 and 1999 Using Hexagon KH-9 Imagery. *Glob. Planet. Change* 128, 1–13.
<https://doi.org/10.1016/j.gloplacha.2014.11.014>, 2015



800

Pritchard, H.D.: Asia's shrinking glaciers protect large populations from drought stress. *Nature*, 569, 649–654, <https://doi.org/10.1038/s41586-019-1240-1>, 2019

Satylkanov, R.: Ablation of Ice and Snow of Kara-Batkak Glacier and its Impact on River Flow. *Journal of Climate Change*, 4(2), 1–14, <https://doi.org/10.3233/jcc-180009>, 2018

Savoskul, O. S. and Solomina, O. N.: Late-Holocene glacier variations in the frontal and inner ranges of Tian Shan, central Asia. *Holocene*, 6(1), 25–3, <https://doi.org/10.1177/095968369600600>, 1996

810 Shahgedanova, M., Afzal, M., Hagg, W., Kapitsa, V., Kasatkin, N., Mayr, E., Rybak, O., Saidaliyeva, Z., Severskiy, I., Usmanova, Z., Wade, A., Yaitskaya, N., and Zhumabayev, D.: Emptying Water Towers? Impacts of Future Climate and Glacier Change on River Discharge in the Northern Tien Shan, Central Asia, *Water*, 12, 627, <https://doi.org/10.3390/w12030627>, 2020

815 Shean, D.E., Bhushan, S., Montesano, P., Rounce, D.R., Arendt, A. and Osmanoglu, B.: A systematic, regional assessment of high mountain Asia glacier mass balance. *Frontiers in Earth Science*, 7, 363, <https://doi.org/10.3389/feart.2019.00363>, 2020

Solomina, O., Barry, R. and Bodnya, M.: The Retreat of Tien Shan Glaciers (Kyrgyzstan) since the Little Ice Age Estimated from Aerial Photographs, Lichenometric and Historical Data. *Geografiska Annaler Series A Physical Geography*, 86, 205–215. <https://doi.org/10.1111/j.0435-3676.2004.00225.x>, 2004

825 Solomina, O., Maximova, O. and Cook, E.: *Picea Schrenkiana* Ring Width and Density at the Upper and Lower Tree Limits in the Tien Shan Mts (Kyrgyz Republic) as a Source of Paleoclimatic Information. *Geogr. Environ. Sustain.* 7 (1), 66–79. <https://doi.org/10.24057/2071-9388-2014-7-1-66-79>, 2014

Sorg, A., Bolch, T., Stoffel, M., Solomina, O., and Beniston, M.: Climate change impacts on glaciers and runoff in Tien Shan (Central Asia), *Nat. Clim. Change*, 2, 725–731, <https://doi.org/10.1038/nclimate1592>, 2012

830 Takeuchi, N., Fujita, K., Aizen, V. B., Narama, C., Yokoyama, Y., Okamoto, S., Naoki, K., and Kubota, J.: The disappearance of glaciers in the Tien Shan Mountains in Central Asia at the end of Pleistocene, *Quaternary Science Revision*, 103, 26–33, <https://doi.org/10.1016/j.quascirev.2014.09.006>, 2014



- 835 Thompson, L. G., Mosley-Thompson, E., Davis, M., Lin, P. N., Yao, T., Dyurgerov, M., and Dai, J.: Recent warming: ice core evidence from tropical ice cores with emphasis on Central Asia, *Global Planet. Change*, 7, 145–156, [https://doi.org/10.1016/0921-8181\(93\)90046-Q](https://doi.org/10.1016/0921-8181(93)90046-Q), 1993
- 840 Van Tricht, L., Huybrechts, P., Van Breedam, J., Fürst, J., Rybak, O., Satylkanov, R., Ermenbaiev B., Popovnin V., Neyns, R., Paice C.M. and Malz, P.: Measuring and inferring the ice thickness distribution of four glaciers in the Tien Shan, Kyrgyzstan. *Journal of Glaciology*, 67(262), 269–286. <https://doi.org/10.1017/jog.2020.104>, 2021a
- 845 Van Tricht L., Paice C.M., Rybak O., Satylkanov R., Popovnin V., Solomina O. and Huybrechts P.: Reconstruction of the Historical (1750–2020) Mass Balance of Bordu, Kara-Batkak and Sary-Tor Glaciers in the Inner Tien Shan, Kyrgyzstan. *Frontiers in Earth Science*, 9, <https://doi.org/10.3389/feart.2021.734802>, 2021b
- 850 Van Tricht, L., Huybrechts, P., Van Breedam, J., Vanhulle, A., Van Oost, K., and Zekollari, H.: Estimating surface mass balance patterns from unoccupied aerial vehicle measurements in the ablation area of the Morteratsch–Pers glacier complex (Switzerland), *The Cryosphere*, 15, 4445–4464, <https://doi.org/10.5194/tc-15-4445-2021>, 2021c.
- 855 Venukov, M.I.: Ocherki Zailiiskogo kraja i Prichuiskoi strain [Essays of Zailiiski region and Prichuiskii country]. *Izv. Russ. Geograf. Obsheh., Rossiiskaya Akademiya Nauk*, 4, 35–61, 1861
- 860 Zekollari, H., Huybrechts, P., Fürst, J. J., Rybak, O., and Eisen, O.: Calibration of a higher-order 3-D ice-flow model of the Morteratsch glacier complex, Engadin, Switzerland, *Ann. Glaciol.*, 54, 343–351, <https://doi.org/10.3189/2013AoG63A434>, 2013
- 865 Zekollari, H., Fürst, J., and Huybrechts, P.: Modelling the evolution of Vadret da Morteratsch, Switzerland, since the Little Ice Age and into the future, *J. Glaciol.*, 60, 1155–1168, <https://doi.org/10.3189/2014JoG14J053>, 2014
- Zekollari, H. and Huybrechts, P.: On the climate–geometry imbalance, response time and volume–area scaling of an alpine glacier: insights from a 3-D flow model applied to Vadret da Morteratsch, Switzerland, *Ann. Glaciol.*, 56, 51–62, <https://doi.org/10.3189/2015AoG70A921>, 2015
- Zekollari, H., Huybrechts, P., Noël, B., van de Berg, W. J., and van den Broeke, M. R.: Sensitivity, stability and future

<https://doi.org/10.5194/egusphere-2022-1441>
Preprint. Discussion started: 17 February 2023
© Author(s) 2023. CC BY 4.0 License.



evolution of the world's northernmost ice cap, Hans Tausen Iskappe (Greenland), *The Cryosphere*, 11, 805–825,
<https://doi.org/10.5194/tc-11-805-2017>, 2017